Quantum Emulation of Coherent Backscattering in a System of Superconducting Qubits

Ana Laura Gramajo,[1,2,*] Dan Campbell,[1] Bharath Kannan,[1] David K. Kim,[3] Alexander Melville,[3] Bethany M. Niedzielski,[4] Jonilyn L. Yoder,[3] María José Sánchez,[2,5] Daniel Domínguez,[2] Simon Gustavsson,[1] and William D. Oliver[1,3,4]

[1] *Research Laboratory of Electronics, Massachusetts Institute of Technology, Cambridge, Massachusetts 02139, USA*

[2] *Centro Atómico Bariloche and Instituto Balseiro, 8400 San Carlos de Bariloche, Argentina*

[3] *MIT Lincoln Laboratory, 244 Wood Street, Lexington, Kentucky 02420, USA*

[4] *Department of Physics, Massachusetts Institute of Technology, Cambridge Massachusetts 02139, USA*

[5] *Instituto de Nanociencia y Nanotecnología (INN), 8400 San Carlos de Bariloche, Argentina*

(Received 3 January 2020; accepted 20 May 2020; published 16 July 2020)

In condensed matter systems, coherent backscattering and quantum interference in the presence of time-reversal symmetry lead to well-known phenomena, such as weak localization (WL) and universal conductance fluctuations (UCFs). Here we use multipass Landau-Zener transitions at the avoided crossing of a highly coherent superconducting qubit to emulate these phenomena. The average and standard deviations of the qubit transition rate exhibit a dip and peak when the driving waveform is time-reversal symmetric, analogous to WL and UCFs, respectively. The higher coherence of this qubit enabled the realization of both effects, in contrast to the earlier work by Gustavsson *et al.* [Phys. Rev. Lett. 110, 016603 (2013)], who successfully emulated UCFs, but did not observe WL. This demonstration illustrates the use of nonadiabatic control to implement quantum emulation with superconducting qubits.

DOI: 10.1103/PhysRevApplied.14.014047

I. INTRODUCTION

Studies of mesoscopic disordered structures at cryogenic temperatures exhibit universal phenomena in their electrical conductance arising from the coherent scattering of electrons at random impurities [1–3]. One example is universal conductance fluctuations (UCFs) [3–6], which are strong fluctuations in the conductance—on the order of the quantum unit of conductance—that appear as a function of a parameter, e.g., magnetic field, which effectively alters how the electronic wave function samples the random configuration of scatterers. Another example is weak localization (WL), a quantum correction to the classical conductance that survives disorder averaging under conditions of time-reversal symmetry [7–9]. The result is a dip in the disordered-averaged conductance (equivalently, a peak in the resistance) at zero magnetic field and when spin-orbit effects are negligible, due to the constructive interference between the symmetric forward- and backward-propagating electron waves arising from impurity scattering [6,10]. In the presence of a magnetic field, the time-reversal symmetry—and thus the degeneracy in phase evolution—is lifted for the two paths and the interference leading to the WL effect is abated [6,10]. Studies of WL and UCFs provide a method for investigating phenomena related to phase coherence, coherent backscattering, and time-reversal symmetry, and they have been applied to a wide variety of systems ranging from metals [11] and semiconductors [12] to superconducting solid-state devices [13], quantum dots [14–16], and graphene [17], and even for the scattering of light of disordered media [18–21].

This work implements a quantum emulator of WL and UCFs phenomena using coherent scattering at an avoided crossing present in coupled superconducting qubits. The approach is motivated by earlier work in Ref. [22], where an avoided crossing of a single persistent-current flux qubit was used to represent a coherent scattering impurity. Conceptually, each period of a large-amplitude biharmonic flux signal drives the qubit multiple times through the avoided crossing. Each traversal of the crossing drives the qubit states into quantum superpositions of ground and excited states—Landau-Zener-Stückelberg (LZS) transitions—with output amplitudes related to the size of the avoided crossing, the rate at which the qubit is driven through the crossing, and the resulting quantum interference. The traversals serve as the scattering sites, and

*gramajo.anala@gmail.com

the driven evolution between scattering events accounts for free-evolution phase accumulation of an electron, for example, in a disordered medium. Since the scattering events are imposed by the driving protocol, the time-reversal symmetry (asymmetry) of the system is controlled by the temporal symmetry (asymmetry) of the drive waveform.

Using this approach, Gustavsson *et al.* [22] emulated UCF-type phenomena—analogous to fluctuations observed in electron transport through a disordered mesoscopic system—by describing the qubit-state transition rate to electrical conductance. The authors observed fluctuations in the transition rate to the qubit excited state arising from multiple LZS scattering events when measured as a function of the driving waveform asymmetry. However, the analog of WL localization—a dip in the average transition rate for symmetric driving—was not observed. Subsequent theoretical work by Ferrón *et al.* [23] indicated that both UCFs and WL signatures should be observable if the qubit is operated in a higher phase-coherence regime. Indeed, while the niobium qubit used in Ref. [22] had a large energy relaxation time ($T_1 \approx 20$ μs) and a coherence time ($T_2 \approx 20$ ns) sufficient to observe LZS interference phenomena including Mach-Zehnder-type interferometry [24,25], qubit cooling [26], and amplitude spectroscopy [27,28], the phase coherence time was apparently insufficient to observe WL.

II. EXPERIMENTAL IMPLEMENTATION

In this work, we use coupled aluminum transmon qubits [29] to realize a higher-coherence quantum system with a reasonably sized avoided crossing (approximately equal to 65.4 MHz). We drive the system using a biharmonic waveform—with a specified degree of asymmetry—to emulate electron transport in the presence of multiple scattering events. The resulting transition rate exhibits effects analogous to WL and UCFs in its ensemble-averaged mean and variance, respectively. The experimental results are in agreement with simulations based on a Floquet formalism.

We utilize an effective two-level system encoded in the single-excitation manifold of two capacitively coupled superconducting transmon qubits [30,31] of the X-mon style [32] using asymmetric junctions with a 13:1 area ratio [33]. The individual transmons Q_a and Q_b are well matched in frequency, with maximum frequencies $\omega_a^{\max}/2\pi = 3.8250$ GHz and $\omega_b^{\max}/2\pi = 3.8218$ GHz and minimum frequencies $\omega_a^{\min}/2\pi = 3.5401$ GHz and $\omega_b^{\min}/2\pi = 3.5365$ GHz, respectively, and they are each frequency tunable between the two values by magnetic fluxes Φ_a and Φ_b (see Fig. 1). The qubits are individually coupled to readout resonators at frequencies $\omega_a^{\text{res}}/2\pi = 7.173\,262$ GHz and $\omega_b^{\text{res}}/2\pi = 7.203\,279$ GHz, which are used for qubit state discrimination and provide an additional pathway to implement state preparation using microwave gates.

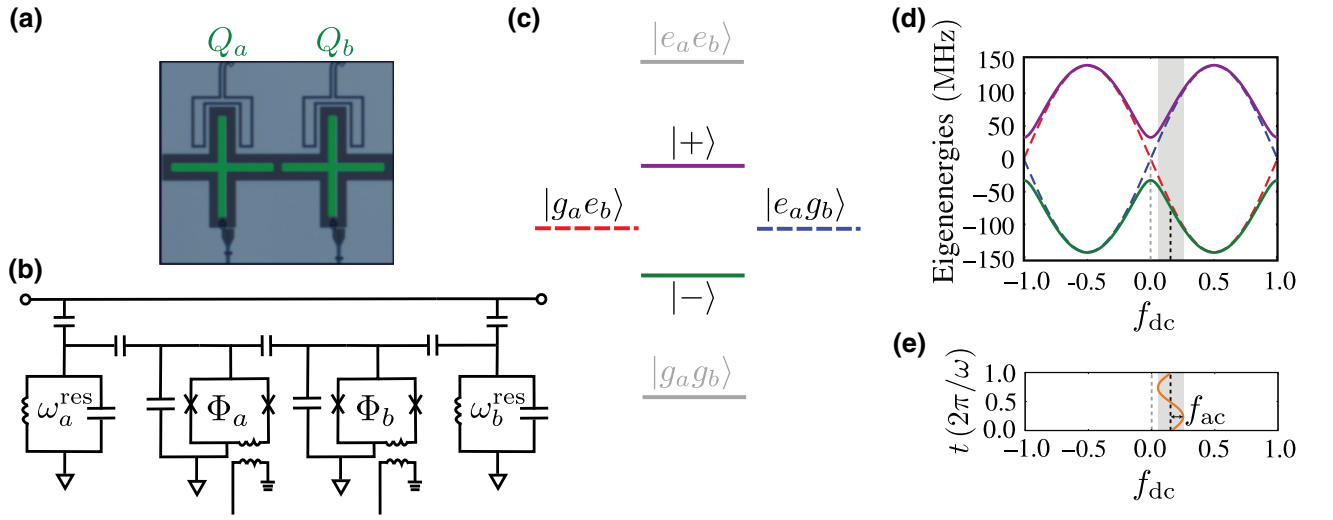

FIG. 1. Experimental device and energy levels. (a) False color micrograph of two capacitively coupled transmon qubits, Q_a and Q_b. (b) Circuit schematic. Qubits $Q_{a,b}$ each have individual control lines used to differentially implement (see the text) a static (f_{dc}) magnetic flux bias and the biharmonic driving protocol (f_{ac}) through the flux biases $\Phi_{a,b}$. Standard microwave gates are used for device initialization, and the qubits are read out by capacitively coupling to individual readout resonators with frequencies $\omega_{a,b}^{\text{res}}$. (c) Energy levels of the two qubits. The red and blue diabatic energies correspond to one excitation of one of the qubits. These levels are frequency tunable using baseband flux control. When degenerate, these levels hybridize to form an avoided crossing of approximately 65.4 MHz. (d) Diabatic energies (dashed lines) and eigenenergies (solid lines) of the one-excitation manifold $\{|e_a g_b\rangle, |g_a e_b\rangle\}$ as a function of f_{dc}. (e) Scattering at the avoided crossing is implemented using a driving pulse $f(t) = f_{\text{dc}} + f_{\text{ac}}(t)$, illustrated here as a sine wave. The driving pulse is applied differentially to each qubit.

The qubits are each flux biased at $\Phi_a \approx \Phi_b \approx 0.25\Phi_0$, where $\Phi_0 = h/2e$ is the superconducting flux quantum, h is Planck's constant, and e is the electron charge. This bias point is approximately midway between maximum and minimum qubit frequencies such that the uncoupled qubit frequencies $\omega_a/2\pi = \omega_b/2\pi = 3.6809$ GHz are degenerate, leading to the energy level structure in the diabatic basis shown in Fig. 1(c). Because of the capacitive qubit-qubit coupling, the diabatic states $|g_a e_b\rangle$ and $|e_a g_b\rangle$ in the single-excitation manifold hybridize to form the eigenfrequencies shown in Fig. 1(c). Within this manifold, we can now write an effective two-level system Hamiltonian of the standard form in the basis $\{|g_a e_b\rangle, |e_a g_b\rangle\}$,

$$\hat{H}_{\rm eff}/\hbar = -\frac{\varepsilon}{2}\hat{\sigma}_z - \frac{\Delta}{2}\hat{\sigma}_x, \tag{1}$$

where $\hbar$ is the reduced Planck constant $h/2\pi$, $\hat{\sigma}_z$ and $\hat{\sigma}_x$ are Pauli matrices, ε is referenced to the location of the avoided crossing, and $\Delta/2\pi = 65.4$ MHz is the transverse coupling strength and, thereby, the size of the avoided crossing.

Excursions about the effective two-level system are driven using a longitudinal flux bias applied differentially to the two qubits, $\delta\Phi(t) = [\Phi_a(t) - \Phi_b(t)]/2 \equiv \delta\Phi_{\rm dc} + \delta\Phi_{\rm ac}(t)$, comprising a time-dependent excursion $\delta\Phi_{\rm ac}$ about a static bias point $\delta\Phi_{\rm dc}$ referenced with respect to the avoided crossing [see Figs. 1(d) and 1(e)]. The drive is parameterized as a unitless reduced flux $f(t) = \delta\Phi(t)/\Phi_0 = f_{\rm dc} + f_{\rm ac}(t)$ by normalizing to the superconducting flux quantum Φ_0 [24,34]. Because of the large area ratio of the junctions, the diabatic frequency ε in Eq. (1) is approximately sinusoidal (see Appendix A) and represents the response of the system to the drive $f(t)$,

$$\varepsilon(t) \approx \delta\omega \sin[2\pi f(t)], \tag{2}$$

where $\delta\omega = (\bar{\omega}^{\rm max} - \bar{\omega}^{\rm min})/2$, with $\bar{\omega}^{\rm max/min}$ the average of $\omega_a^{\rm max/min}$ and $\omega_b^{\rm max/min}$, respectively, yielding $\delta\omega/2\pi = 0.1426$ GHz. The instantaneous frequency of the driven two-level system is $\Omega(t) = \sqrt{\varepsilon^2(t) + \Delta^2}$.

To simulate mesoscopic conductance effects, following Ref. [22], we drive the system with a biharmonic signal,

$$f(t) = f_{\rm dc} + f_{\rm ac}[\cos(\omega t) + \cos(2\omega t + \alpha)], \tag{3}$$

with $\omega/2\pi = 10$ MHz, an excursion amplitude $f_{\rm ac} = 0.1$, and a phase α that parameterizes the waveform symmetry and thereby the time-reversal symmetry of the system [see Fig. 2(a)]. As with Ref. [22], the analogy is based on Landau-Zener transitions and the qubit evolution as a phase-space analog of an optical Mach-Zehnder interferometer [24], where each Landau-Zener transition depicts a scattering event. In Fig. 2(b) we display the energy evolution of the qubit during the drive, where each of the interference phases $\varphi = \int \Omega(t)dt$ are given by the shaded area between scattering events. Although the biharmonic nature of $f(t)$ will drive the system through the avoided crossing up to four times per period for specific values of $f_{\rm dc}$, the accumulated interference phases φ are time-reversal symmetric for $\alpha = 0$ [Fig. 2(b), $\alpha = 0$]. In this case, the qubit trajectories will pick up the same phase during the driven evolution, and they will, therefore, interfere constructively over multiple periods. However, for $\alpha \neq 0$, the waveform is no longer time symmetric, and so the interference phases are similarly no longer time symmetric

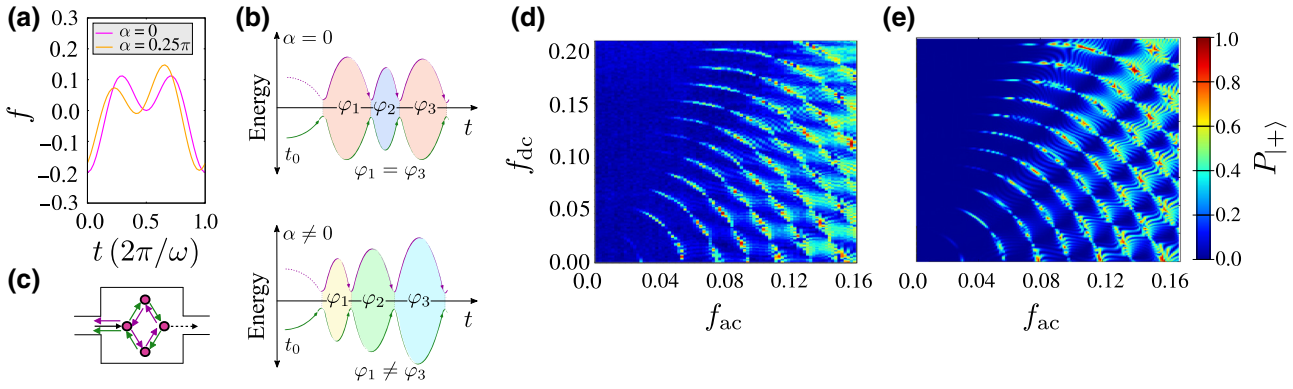

FIG. 2. Biharmonic driving. (a) Partial period of the biharmonic signal that drives the qubit system multiple times through the avoided crossing for $f_{\rm dc} = 0, f_{\rm ac} = 0.1, \alpha = 0$ (magenta line), and $\alpha = 0.25\pi$ (orange line); see Eq. (3). (b) Evolution of the system's eigenenergy and resulting phase accrual for symmetric ($\alpha = 0$) and nonsymmetric ($\alpha \neq 0$) biharmonic signals driving the system through the avoided crossing four times. For $\alpha = 0$, the system acquires phases in a time-symmetric manner, $\varphi_1 = \varphi_3$. For $\alpha \neq 0$, the phase accrual is no longer time symmetric. (c) Illustration of coherent forward and back scattering in a disordered condensed matter system. (d) Experimental measurement of the excited-state ($|+\rangle$) occupation probability (color scale) as a function of $f_{\rm dc}$ and $f_{\rm ac}$, over 20 driving periods, with $\alpha = 0$. (e) The corresponding numerical simulation.

[Fig. 2(b), $\alpha = 0.25\pi$]. The sequential temporal scattering events mimic the spatial scattering in a disordered condensed matter system [Fig. 2(c)].

The control and measurement protocol consists of the following steps: (1) the qubits are prepared in the two-level system ground state at flux $f_{\rm dc}$; (2) the drive signal [Eq. (3)] is applied to the two-level system for an interval of time (a number of periods of the driving field); and (3) the system state is determined by reading out each qubit. Qubit-state readout in the system eigenbases is implemented by adiabatically shifting the qubits away from the avoided crossing region into a region where the uncoupled, diabatic basis states $|g_a e_b\rangle$ and $|e_a g_b\rangle$ are essentially identical to the eigenstates. Measuring the individual qubits in this regime are used to infer the occupation probability of the eigenstates [35,36].

Using this driving protocol, an analog to the conductance of a mesoscopic system can be emulated by measuring the qubit transition rate W, the rate at which population transitions between ground and excited states of the avoided crossing [22]. Multiple sequential passes through a single avoided crossing mimic the scattering amongst a spatial distribution of scatterers [Fig. 2(c)]. The phase accumulated between scattering events is dictated by the symmetry and amplitude of the driving waveform. Unique values of $f_{\rm dc}$ in Eq. (3) mimic different scattering configurations, $f_{\rm ac}$ effectively sets transition probabilities and the scattering phases, and the parameter α sets the time-reversal symmetry. The average transition rate $\langle W\rangle$—the analog of average conductance—is then obtained by ensemble averaging the measured transition rate over all $f_{\rm dc}$ realizations. See Appendix C for more details.

III. RESULTS AND DISCUSSION

We plot the excited-state population of the two-level system as a function of $f_{\rm dc}$ and $f_{\rm ac}$ [Fig. 2(d)]. The driving field extends for 20 periods with each period being time symmetric ($\alpha = 0$). Each period is approximately 100 ns, and thus 20 periods is approximately 2 μs smaller than the independently measured coherence times of the two-level system that vary between 4 and 20 μs, depending on the bias point. Thus, the system remains coherent during the entire driving protocol. A numerical simulation of the time-dependent Schrödinger equation [Fig. 2(e)] for these driving parameters is in good agreement with the experimental results; see Appendix B. The periodic structure observed in Figs. 2(d) and 2(e) arises from LZS interference upon scattering at the avoided crossings, analogous to a multipass optical interferometer [24,25,27,37].

In order to obtain the transition rate W, we measure the excited-state population $P_{|+\rangle}(t)$ as a function of time t and static magnetic flux $f_{\rm dc}$ for a fixed excursion amplitude $f_{\rm ac} = 0.1\Phi_0$ and a specific value of asymmetry parameter α. As an example, in Fig. 3(a) we show the measurements of $P_{|+\rangle}(t)$ for $\alpha = 0$. The asymmetry of the resulting excited-state population for plus and minus values of $f_{\rm dc}$ results from the driving protocol: at $t = 0$, the temporal periodic waveform moves away from $f_{\rm dc}$ in the same flux direction. The first half-period will therefore either approach or move away from the avoided crossing, depending on whether $f_{\rm dc}$ is positive or negative [27]. This leads to the left-right asymmetry as a function of $f_{\rm dc}$ in Fig. 3(a).

We then fit $P_{|+\rangle}(t)$ for each value of $f_{\rm dc}$ using the function

$$P_{|+\rangle}(t) = P_T \sin(\Omega_T t + \varphi) + P_0 \tag{4}$$

with P_T, Ω_T, φ, and P_0 the fitting parameters. The transition rate can then be computed from the expression

$$W(f_{\rm dc}) = \left|\frac{dP_{|+\rangle}(t)}{dt}\right|_{t=0} \propto |P_T \Omega_T|. \tag{5}$$

The quantity $|P_T\Omega_T|$ serves as a proxy for the transition rate. In Fig. 3(b) we show an example fitting of $P_{|+\rangle}(t)$ for $f_{\rm dc} = -0.0126\Phi_0$ and $\alpha = 0$, from which $W(f_{\rm dc})$ is extracted. The resulting transition rate W for each value

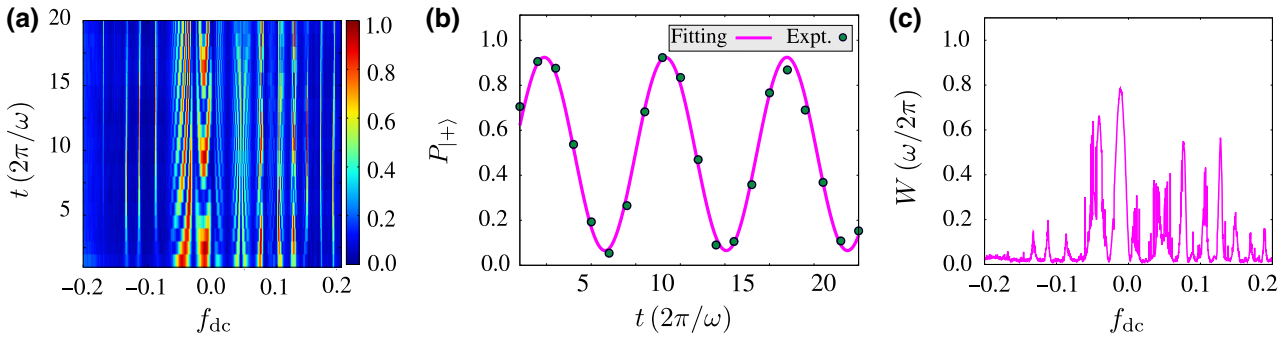

FIG. 3. Transition rate. (a) Measurement of the occupation probability $P_{|+\rangle}$ as a function of time t and bias point $f_{\rm dc}$ with $\alpha = 0$. (b) Temporal coherent oscillations in $P_{|+\rangle}$ at $f_{\rm dc} = -0.0126$ due to Landau-Zener-Stückelberg transitions at the avoided crossing are fitted [Eq. (4)] to extract the transition rate W [Eq. (5)]. (c) Transition rate W plotted as a function of $f_{\rm dc}$ from the data in (a).

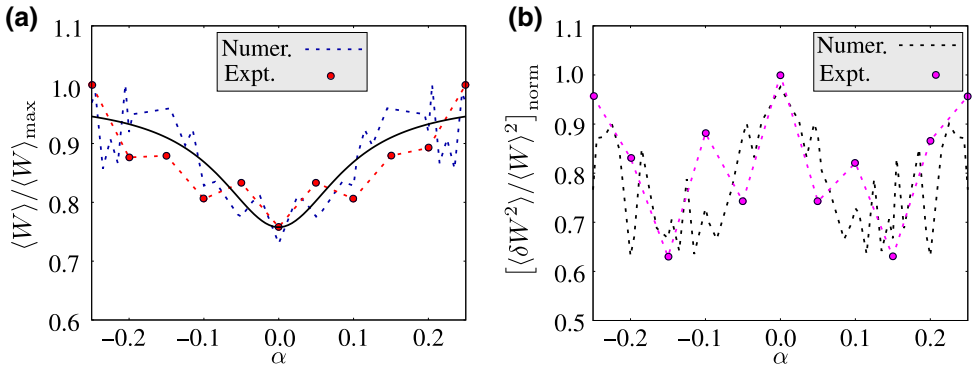

FIG. 4. First- and second-order statistics of the transition rate: WL and UCFs. (a) Experimental and numerical results of the normalized transition rate $\langle W\rangle/\langle W\rangle_{\max}$ as a function of the asymmetry parameter α. Here $\langle W\rangle$ is the transition rate ensemble averaged over all $f_{\rm dc}$ values [Fig. 3(c)] for fixed α, and $\langle W\rangle_{\max}$ is the corresponding maximum value for each case. The bold line is a fit to the data based on the theoretically expected dependence in the WL regime (see the text). (b) Experimental and numerical results for the normalized variance $[\langle \delta W^2\rangle/\langle W\rangle^2]_{\rm norm} = [(\langle W^2\rangle - \langle W\rangle^2)/\langle W\rangle^2]_{\rm norm}$. The normalization $\langle \delta W^2\rangle/\langle W\rangle^2$ is performed in the same manner as in Ref. [23]. There is an extra normalization $[\langle \delta W^2\rangle/\langle W\rangle^2]_{\rm norm} = [\langle \delta W^2\rangle/\langle W\rangle^2]/[\langle \delta W^2\rangle/\langle W\rangle^2]_{\max}$, with $[\langle \delta W^2\rangle/\langle W\rangle^2]_{\max}$ the corresponding maximum value for each case.

of $f_{\rm dc}$ for $\alpha = 0$ is plotted in Fig. 3(c). Averaging over all values of $f_{\rm dc}$ (all scattering configurations) leads to the ensemble-averaged transition rate

$$\langle W\rangle = \frac{1}{N}\sum_{n=1}^{N} W(f_{\rm dc}[n]), \tag{6}$$

where $\langle\cdot\rangle$ is the ensemble average over $f_{\rm dc}$, n indexes the values of $f_{\rm dc}$, and N is the total number of $f_{\rm dc}$ values. This procedure is then repeated for different values of the symmetry parameter α. The extracted experimental $\langle W\rangle$ for multiple values of α is plotted in Fig. 4(a), along with results from the numerical simulation (see Appendix D for details). Importantly, $\langle W\rangle$ exhibits a dip—weak localization—when time-reversal symmetry ($\alpha = 0$) is imposed. The suppression of the WL correction in the average conductance follows a Lorentzian line shape with the magnetic field B (in a diffusive transport regime [38]). Considering that the parameter α mimics the role of B, we plot in Fig. 4(a) a fit to $\langle W\rangle_\alpha = \tilde{a} - \tilde{b}/[1 + (\alpha/\alpha_c)^2]$, obtaining good agreement with the experimental results, with $\alpha_c = (0.09 \pm 0.03)$ (see Appendixes C and D for a detailed discussion).

We now proceed to extract the variance in the transition rate,

$$\langle \delta W^2\rangle = \langle W^2\rangle - \langle W\rangle^2. \tag{7}$$

The experimental and numerical results [Fig. 4(b)] both exhibit a peak in $\langle \delta W^2\rangle$ for $\alpha = 0$, corresponding to the analog of UCFs. We obtain $\langle \delta W^2\rangle/\langle W\rangle^2 \approx 0.6$, which is in quite good agreement with theoretical predictions for disordered systems with many scatterers (see Appendix D for further analysis).

IV. CONCLUSIONS

An important outcome of this work is the emulation of both WL-type and UCF-type phenomena via coherent scattering at the avoided crossing of a strongly driven qubit system. Although such UCF-type phenomena were previously reported in Ref. [22], WL was not observed at that time. The reason was ultimately traced to the relatively short coherence time of the device used in that work, and not an aspect of the driving protocol, as clarified in Ref. [23]. The present work therefore serves as experimental confirmation of the theory presented in Ref. [23], and it emphasizes two additional interesting points. First, even with only a very small number of scattering events, it is possible to emulate behavior that is reminiscent of the well-studied UCFs and WL phenomena observed in disordered mesoscopic systems with many more scatterers. Second, while WL and UCFs are both quantum coherent phenomena, WL is apparently more sensitive to quantum coherence in this driven system, requiring a device with higher coherence to manifest itself.

ACKNOWLEDGMENTS

This research was funded by the Office of the Director of National Intelligence (ODNI), Intelligence Advanced Research Projects Activity (IARPA) under Air Force Contract No. FA8721-05-C-0002. The views and conclusions contained herein are those of the authors and should not be interpreted as necessarily representing the official policies or endorsements, either expressed or implied, of ODNI, IARPA, or the US Government. A.L.G., D.D., and M.J.S. are funded by CNEA, CONICET (PIP11220150100756), UNCuyo (P 06/C455), and ANPCyT (PICT2014-1382, PICT2016-0791).

APPENDIX A: SINUSOIDAL APPROXIMATION FOR THE DIABATIC FREQUENCY ε

In this section, we derive the sinusoidal expression

$$\varepsilon(t) \approx \delta\omega \sin[2\pi f_{\rm dc}(t)], \tag{A1}$$

where $\delta\omega = (\bar{\omega}^{\rm max} - \bar{\omega}^{\rm min})/2$, with $\bar{\omega}^{\rm max/min}$ the average of $\omega_a^{\rm max/min}$ and $\omega_{\rm b}^{\rm max/min}$; see Sec. II for further details. In particular, we bias the qubits at $\pm 0.25\Phi_0$, as we show in Fig. 1, which allows us to write the Eq. (A1).

To obtain Eq. (A1), we start by considering the general expression [33] for the diabatic frequency of one of the transmons, say Q_a,

$$\varepsilon_a(t) = \sqrt{E_{J\Sigma,a}\cos[\pi f_{\rm dc}(t)]\sqrt{1 + d^2\tan[\pi f_{\rm dc}(t)]^2}}\,, \tag{A2}$$

where $E_{J\Sigma,a} = \sqrt{E_{J1,a} + E_{J2,a}}$, with $E_{J1,a}$ and $E_{J2,a}$ the Josephson energies of each junction, satisfying $E_{J1,a} = \alpha E_{J2,a}$ and $E_{J1,a} \gg E_{J2,a}$. The parameter d satisfies the relation

$$d = \frac{\alpha - 1}{\alpha + 1}. \tag{A3}$$

Furthermore, since we are working in the limit of the large area ratio of α of the junctions, then $d \to 1$. Note that the two transmons are well matched, with maximum frequencies $\omega_a^{\rm max}/2\pi = 3.8250$ GHz and $\omega_b^{\rm max}/2\pi = 3.8218$ GHz and minimum frequencies $\omega_a^{\rm min}/2\pi = 3.5401$ GHz and $\omega_b^{\rm min}/2\pi = 3.5365$ GHz. Therefore, for the moment, we focus on only one transmon.

We begin with the expression

$$E_{J\Sigma,a}\cos(x)\sqrt{1 + d^2\tan^2(x)}, \qquad x = \pi f_{\rm dc}(t), \tag{A4}$$

corresponding to the function inside the square root of Eq. (A2). Taking the limit $d \to 1$, we obtain

$$\lim_{d\to 1}\sqrt{1 + d^2\tan^2(x)} \to \sqrt{\sec(x)^2} + (d-1)\frac{\tan(x)^2}{\sqrt{\sec(x)^2}} + O[(d-1)^2]. \tag{A5}$$

Note that, to obtain the rhs term of Eq. (A5), we performed a Taylor series expansion around $d = 1$, i.e.,

$$f(d,x) = \sqrt{1 + d^2\tan^2(x)} = \sum_{n=0}^{\infty}\frac{\partial^n f(d,x)}{\partial^n d}\frac{(d-1)^n}{n!}, \qquad n \in \mathbb{N}, \tag{A6}$$

keeping only the first two terms.

Substituting (A5) into (A4), we obtain

$$E_{J\Sigma,a}\cos(x)\left(\sec(x) + (d-1)\frac{\tan(x)^2}{\sec(x)}\right) \to E_{J\Sigma,a} + E_{J\Sigma,a}(d-1)\sin^2(x). \tag{A7}$$

Equation (A2) then becomes

$$\varepsilon_a(t) \approx \sqrt{E_{J\Sigma,a} + E_{J\Sigma,a}(d-1)\sin^2(x)}. \tag{A8}$$

Going a step further and using a Taylor series expansion, we obtain

$$\lim_{d\to 1}\sqrt{b + (d-1)a} \to \sqrt{b} + \frac{a}{2\sqrt{b}}(d-1) + O[(d-1)^2], \tag{A9}$$

where $b = E_{J\Sigma,a}$ and $a = E_{J\Sigma,a}\sin(x)^2$. Equation (A8) can be written as

$$\varepsilon_a(t) \approx \sqrt{E_{J\Sigma,a}} + \frac{\sqrt{E_{J\Sigma,a}}(d-1)}{2}\sin^2(x). \tag{A10}$$

Furthermore, using the trigonometric relation $\sin^2(x) = [1 - \cos(2x)]/2$,

$$\varepsilon_a(t) \approx \sqrt{E_{J\Sigma,a}}\left(1 + \frac{d-1}{4}\right) - \frac{\sqrt{E_{J\Sigma,a}}(d-1)}{4}\cos(2x). \tag{A11}$$

Recalling that $x = \pi f_{\rm dc}$, we have

$$\begin{aligned}\varepsilon_a(t) &\approx \sqrt{E_{J\Sigma,a}}\left(1 + \frac{d-1}{4}\right) - \frac{\sqrt{E_{J\Sigma,a}}(d-1)}{4}\cos[2\pi f_{\rm dc}(t)],\\ &\approx \sqrt{E_{J\Sigma,a}}\left(1 - \frac{1-d}{4}\right) + \frac{\sqrt{E_{J\Sigma,a}}(1-d)}{4}\cos[2\pi f_{\rm dc}(t)].\end{aligned} \tag{A12}$$

We now proceed to demonstrate the following relations:

$$\begin{aligned}\sqrt{E_{J\Sigma,a}}\left(1 - \frac{1-d}{4}\right) &\approx \frac{\omega^{\rm max} + \omega^{\rm min}}{2},\\ \frac{\sqrt{E_{J\Sigma,a}}(1-d)}{4} &\approx \frac{\omega^{\rm max} - \omega^{\rm min}}{2}.\end{aligned} \tag{A13}$$

We start with the definitions

$$\begin{aligned}\omega_a^{\rm max} &= \sqrt{E_{J1,a} + E_{J2,a}} = \sqrt{E_{J\Sigma,a}},\\ \omega_a^{\rm min} &= \sqrt{E_{J1,a} - E_{J2,a}}.\end{aligned} \tag{A14}$$

Remember that $E_{J1,a} \gg E_{J2,a}$, with $\alpha = E_{J1,a}/E_{J2,a}$. Moreover, substituting Eq. (A14) into Eq. (A3) we obtain the

contraint

$$\sqrt{d} = \frac{\omega_a^{\min}}{\omega_a^{\max}}. \tag{A15}$$

Thus, substituting (A15) into the rhs of (A13) we obtain

$$\begin{aligned} \frac{\omega_a^{\max} + \omega_a^{\min}}{2} &= \omega_{\max}\frac{1+\sqrt{d}}{2} = \sqrt{E_{J\Sigma,a}}\frac{1+\sqrt{d}}{2}, \\ \frac{\omega_a^{\max} - \omega_a^{\min}}{2} &= \omega_{\max}\frac{1-\sqrt{d}}{2} = \sqrt{E_{J\Sigma,a}}\frac{1-\sqrt{d}}{2}. \end{aligned} \tag{A16}$$

This last expression is quite similar to Eq. (A10), but we need to work a little more to obtain the same equality.

Taking the limit $d \to 1$, we have

$$\lim_{d\to 1}\sqrt{d} \to 1 + \frac{d-1}{2} + O[(d-1)^2]. \tag{A17}$$

Substituting this expression into (A16) we obtain

$$\begin{aligned} \frac{\omega_a^{\max} + \omega_a^{\min}}{2} &\approx \sqrt{E_{J\Sigma,a}}\left(1 - \frac{1-d}{4}\right), \\ \frac{\omega_a^{\max} - \omega_a^{\min}}{2} &\approx \sqrt{E_{J\Sigma,a}}\frac{1-d}{4}. \end{aligned} \tag{A18}$$

Then Eq. (A13) is satisfied.

We finally arrive at the diabatic frequency for the transmon Q_a:

$$\varepsilon_a(t) \approx \frac{\omega_a^{\max} - \omega_a^{\min}}{2}\cos[2\pi f_{\rm dc}(t)] + \frac{\omega_a^{\max} + \omega_a^{\min}}{2}. \tag{A19}$$

Following the same procedure, the diabatic frequency for the transmon Q_b is

$$\varepsilon_b(t) \approx \frac{\omega_b^{\max} - \omega_b^{\min}}{2}\cos[2\pi f_{\rm dc}(t)] + \frac{\omega_b^{\max} + \omega_b^{\min}}{2}, \tag{A20}$$

Furthermore, we choose to work with the average diabatic frequency $\varepsilon(t) = [\varepsilon_{\rm a}(t) + \varepsilon_{\rm b}(t)]/2$, since the transmon frequencies match quite well, $\omega_a^{\rm max/min} \approx \omega_b^{\rm max/min}$. Finally, we obtain

$$\begin{aligned} \varepsilon(t) &\approx \frac{\bar{\omega}^{\max} - \bar{\omega}^{\min}}{2}\cos[2\pi f_{\rm dc}(t)] + \frac{\bar{\omega}^{\max} + \bar{\omega}^{\min}}{2}, \\ &\approx \delta\omega\cos[2\pi f_{\rm dc}(t)] + \overline{\omega}. \end{aligned} \tag{A21}$$

Note 1: The numerical results presented in our work have been performed using the propagator method [39]. Since the effective Hamiltonian is periodic in time, we can further use Floquet formalism [37] to solve the time evolution of the system.

Without going into technical details, the system dynamics can be computed by solving the time evolution of the propagator $U(t+\tau, t)$, where τ is the period of the system Hamiltonian. If the Hamiltonian can be decomposed as $\hat{H}_{\rm eff}(t) = \hat{H}_0 + \hat{V}(t)$ then $U(t+\tau, t)$ can be factorized into a kinetic and a potential part. Thus, we obtain

$$\begin{aligned} U(t+\delta t, t) &= e^{-i\hat{H}_0(\delta t/2)}e^{-i\hat{V}(t+\delta t/2)\delta t}e^{-i\hat{H}_0(\delta t/2)} \\ &= \Pi_{n=0}^{N-1}U[(n+1)\delta t, n\delta t] \end{aligned} \tag{A22}$$

with $\delta t = \tau/N$ the time interval. Such factorization carries several difficulties when considering the full expression of $\varepsilon(t)$ (A2), which is why we employ the approximate Eq. (A1).

Note 2: To obtain such numerical and analytical results, for convenience, we let

$$\varepsilon(t) \approx \delta\omega\sin[2\pi f_{\rm dc}(t)], \tag{A23}$$

where $\delta\omega = (\overline{\omega}_{\max} - \overline{\omega}_{\min})/2$, and we let $\cos[2\pi f_{\rm dc}(t)] \to \sin[2\pi f_{\rm dc}(t)]$. By doing this, we set the locations of the avoided crossings Δ at $n\Phi_0$, $n \in \mathbb{Z}$. In particular, the choice of sine references $\varepsilon = 0$ at the avoided crossing. The corresponding experimental value of $\overline{\omega}$ is $\bar{\omega}/2\pi = 3.6809$ GHz.

APPENDIX B: LANDAU-ZENER-STÜCKELBERG INTERFEROMETRY WITH SINGLE DRIVING: SLOW PASSAGE LIMIT

In this section, we briefly analyze the system dynamics of our encoded qubit driven by a single microwave field. In this way, we present experimental and numerical results along with a short analytical description.

As presented in Sec. II, the system of work can be modeled as an effective two-level system driven by an external periodic signal described by the effective Hamiltonian

$$\hat{H}_{\rm eff}(t)/\hbar = -\frac{\varepsilon(t)}{2}\hat{\sigma}_z - \frac{\Delta}{2} \tag{B1}$$

with $\varepsilon(t)$ defined in Eq. (A23), $f(t) = f_{\rm dc} + f_{\rm ac}(t)$, and $f_{\rm ac}(t)$ the external driving. While $f_{\rm ac}(t)$ can take any form, in this section we only consider the case of single driving, $f_{\rm ac}(t) = f_{\rm ac}\cos(\omega t)$. Note that the Hamiltonian (B1) is written in the manifold basis $\{|g_a e_b\rangle, |e_a g_b\rangle\}$. The corresponding energy spectrum as a function of $f_{\rm dc}$ is plotted in Fig. 5(a). The spectrum displays a periodic behavior in terms of $f_{\rm dc}$, where the avoided crossings are periodically located at $f_{\rm dc} = n\Phi_0$, $n \in \mathbb{Z}$.

In Fig. 5(b) we show the measurement of the LZS interferometric pattern [37], plotting the transition probability $P_{|+\rangle}(t_{\rm exp})$ as a function of $f_{\rm dc}$ and $f_{\rm ac}$, after one period of

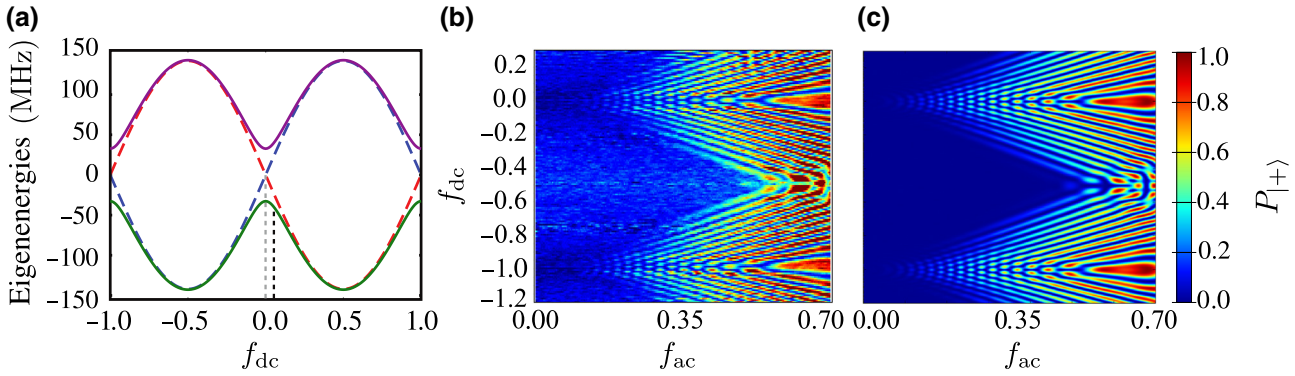

FIG. 5. Resonance pattern of the transition probability. (a) Plot of the energy levels in an extended range of f_{dc}. When the qubit is tuned near an avoided crossing and it is weakly driving, the resonance pattern obeys the dynamics presented in Eq. (B2). When the qubit is tuned near $f_{dc} = 0.5\Phi_0$ and it is strongly driving ($f_{dc} > 0.35\Phi_0$), the transition probability in the space [f_{ac},f_{dc}] manifests another kind of resonance pattern due to the presence of a second avoided crossing. (b) Transition probability measurement $P_{|+\rangle}(t_{exp})$ in terms of f_{dc} and f_{ac}. (c) Numerical results.

the driving $t_{exp} = 2\pi/\omega$. The system has been initially prepared in the ground state $|-\rangle$ for each f_{dc} value. In Fig. 5(c) we present the corresponding numerical simulation results obtained by solving the Schrödinger equation. As can be seen from Fig. 5(c), the experimental results agree quite well with the numerical results.

The calculation of an analytic expression for the time evolution of the transition probability involves several difficulties. As such, it is helpful to use different theoretical approaches to describe the dynamics. Since the driving frequency $\omega/2\pi \approx 10$ MHz is smaller than the minimum energy splitting $\Delta/2\pi \approx 65.4$ MHz, the most suitable approach corresponds to the slow limit passage [37]. In this regime, the interference fringes in the transition probability satisfy the resonance condition

$$\xi_1 + \xi_2 = k\pi \quad \text{for all } k \in \mathbb{Z}, \tag{B2}$$

where $\xi_1 = \int_{t_1}^{t_2} \Omega(t)dt$ and $\xi_2 = \int_{t_2}^{t_1+2\pi/\omega} \Omega(t)dt$ with $\Omega(t) = \sqrt{\varepsilon(t)^2 + \Delta^2}/2$. Note that the integrals ξ_1 and ξ_2 cannot be easily evaluated. However, the resonance condition describes arcs around the point $(f_{ac},f_{dc}) = (0, n\Phi_0)$, observed in Figs. 5(b) and 5(c) when the qubit is driven quite close to each avoided crossing; see Fig. 5(b) to identify the eigenenergy spectrum.

It should be noted that, for our case, the picture described above [37] is only valid for $f_{ac} \ll 0.5\Phi_0$, when the qubit is driven near each avoided crossing. Beyond the upper bound $f_{ac} \gg 0.5\Phi_0$, the interference pattern as a function of f_{dc} and f_{ac} notably changes, since the geometry of the system becomes relevant in the system dynamics. These effects can be observed in Figs. 5(b) and 5(c) when the qubit is driven too far away from $f_{dc} = 0$, reaching the second avoided crossing; see Fig. 5(a).

APPENDIX C: BREAKING TIME-REVERSAL SYMMETRY: ANALYTICAL CALCULATION OF THE TRANSITION RATE

Similarly to previous results [23,25,27], we can approximately calculate the transition rate from the ground state to the excited state via perturbation theory.

We consider the Hamiltonian system presented in the section above [see Eq. (B1)] with the biharmonic driving $f_{ac}(t) = f_{ac1}\cos(\omega_1 t) + f_{ac2}\cos(\omega_2 t + \alpha)$, where $\omega_1 = \omega$ and $\omega_2 = 2\omega$. In order to simplify the calculations, we work under the assumption that the qubit is only driven near one of the avoided crossings, whereby the Hamiltonian (B1) becomes linear around $f_{dc} = n\Phi_0$. In this way, we work with the simplified Hamiltonian, for $n = 0$,

$$\begin{aligned}\hat{H}'_{\text{eff}}(t)/\hbar &\approx -\frac{2\pi\delta\omega f(t)/\Phi_0}{2}\hat{\sigma}_z - \frac{\Delta}{2}\hat{\sigma}_x \\ &\approx -\frac{h(t)}{2}\hat{\sigma}_z - \frac{\Delta}{2}\hat{\sigma}_x.\end{aligned} \tag{C1}$$

Here

$$h(t) = 2\pi\delta\omega f(t) = \varepsilon_0 + g(t),$$

where

$$\varepsilon_0 = 2\pi\delta\omega f_{dc}$$

and

$$g(t) = 2\pi\delta\omega\tilde{f}(t) = A_1\cos(\omega_1 t) + A_2\cos(\omega_2 t + \alpha)$$

with $A_1 = 2\pi\delta\omega f_{ac1}$ and $A_2 = 2\pi\delta\omega f_{ac2}$.

Applying the unitary transformation $\hat{R} = e^{-i\phi(t)\sigma_z^{(i)}/2}$, $\phi(t) = \int_0^t h(t)\,dt$, to the linearized Hamiltonian (C1), we

obtain

$$\hat{\mathcal{H}}(t) = -\frac{\Delta(t)}{2}\hat{\sigma}_+ - \frac{\Delta(t)^*}{2}\hat{\sigma}_- \tag{C2}$$

with $\Delta(t) = \Delta e^{-i\phi(t)}$. Note that this procedure has transformed the problem to the interaction picture, corresponding to a rotation of the Hamiltonian into a rotating framework.

We define the transition rate between the ground $|-\rangle$ and the excited $|+\rangle$ states (diabatic basis) as

$$W = \frac{dP_{|+\rangle}(t)}{dt} = \frac{dP_{|-\rangle\to|+\rangle}(t)}{dt}, \tag{C3}$$

where $P_{|-\rangle\to|+\rangle} = |\langle -|U_I(t,0)|+\rangle|^2$ is the transition probability. That is,

$$W = \frac{d}{dt}|\langle -|U_I(t,0)|+\rangle|^2. \tag{C4}$$

Under the assumption that $\Delta \to 0$, the evolution operator can be expanded to first order in Δ [23,25,27], thus obtaining

$$U_I(t,0) = 1 - i\int_0^t \hat{\mathcal{H}}(\tau)\, d\tau + \mathcal{O}(\Delta^2). \tag{C5}$$

Neglecting the $\mathcal{O}(\Delta^2)$ terms and substituting Eq. (C5) into Eq. (C4), the rate of transition can be expressed as

$$\begin{aligned} W &= \frac{d}{dt}\left|\int_0^t \langle -|\hat{\mathcal{H}}(\tau)|+\rangle d\tau\right|^2 \\ &\equiv \lim_{t\to\infty}\frac{1}{t}\left|\int_0^t \langle -|\hat{\mathcal{H}}(\tau)|+\rangle d\tau\right|^2. \end{aligned} \tag{C6}$$

Using Eq. (C2) and expanding the states $\{|-\rangle, |+\rangle\}$ in terms of the manifold basis $\{|g_a e_b\rangle, |e_a g_b\rangle\}$ as

$$\begin{aligned} |-\rangle &= \cos\left(\frac{\chi}{2}\right)|g_a e_b\rangle + \sin\left(\frac{\chi}{2}\right)|e_a g_b\rangle, \\ |+\rangle &= -\sin\left(\frac{\chi}{2}\right)|g_a e_b\rangle + \cos\left(\frac{\chi}{2}\right)|e_a g_b\rangle, \end{aligned} \tag{C7}$$

with $\chi = \arctan(\Delta/\varepsilon_0)$, Eq. (C6) becomes

$$\begin{aligned} W &= \lim_{t\to\infty}\frac{1}{t}\left|\int_0^t \left[\cos^2\left(\frac{\chi}{2}\right)\Delta(\tau) - \sin^2\left(\frac{\chi}{2}\right)\Delta(\tau)^*\right]d\tau\right|^2 \\ &= \lim_{t\to\infty}\frac{1}{t}\left|\cos^2\left(\frac{\chi}{2}\right)\int_0^t \Delta(\tau)d\tau \right. \\ &\quad \left. - \sin^2\left(\frac{\chi}{2}\right)\int_0^t \Delta(\tau)^* d\tau\right|^2. \end{aligned} \tag{C8}$$

For simplicity, we define the amount $\tilde{P}_{|a\rangle\to|b\rangle}(t) \in \mathbb{C}$ as

$$\tilde{P}_{|a\rangle\to|b\rangle}(t) = \int_0^t \langle a|\hat{\mathcal{H}}(\tau)|b\rangle d\tau. \tag{C9a}$$

$$\begin{aligned} P_{|a\rangle\to|b\rangle}(t) &= \left|\int_0^t \langle a|\hat{\mathcal{H}}(\tau)|b\rangle d\tau\right|^2 \\ &= |\tilde{P}_{|a\rangle\to|b\rangle}(t)|^2, \end{aligned} \tag{C9b}$$

Applying this definition to our case, we obtain

$$\begin{aligned} \tilde{P}_{|g_a e_b\rangle\to|e_a g_b\rangle}(t) &= \int_0^t \Delta(\tau)d\tau, \\ \tilde{P}_{|e_a g_b\rangle\to|g_a e_b\rangle}(t) &= \int_0^t \Delta(\tau)^* d\tau. \end{aligned} \tag{C10}$$

Substituting Eq. (C10) into Eq. (C8) we obtain

$$\begin{aligned} W = \lim_{t\to\infty}\frac{1}{t}\left|\cos^2\left(\frac{\chi}{2}\right)\tilde{P}_{|g_a e_b\rangle\to|e_a g_b\rangle}(t)\right. \\ \left. - \sin^2\left(\frac{\chi}{2}\right)\tilde{P}_{|e_a g_b\rangle\to|g_a e_b\rangle}(t)\right|^2. \end{aligned} \tag{C11}$$

Note that the term $|\cos^2(\chi/2)\tilde{P}_{|g_a e_b\rangle\to|e_a g_b\rangle} - \sin^2(\chi/2)\tilde{P}_{|e_a g_b\rangle\to|g_a e_b\rangle}|^2$ is similar to the expression of the surviving probability when two different paths interfere, that is, $P_s = |A_{\text{path},1} - A_{\text{path},2}|^2$ with $A_{\text{path},i} \in \mathbb{C}$ the quantum amplitude of each path. For our case, we can identify $A_{\text{path},1} \leftrightarrow \tilde{P}_{|g_a e_b\rangle\to|e_a g_b\rangle}(t)$ and $A_{\text{path},2} \leftrightarrow \tilde{P}_{|e_a g_b\rangle\to|g_a e_b\rangle}(t)$.

Now we proceed to expand Eq. C11. We have

$$\begin{aligned} W = \lim_{t\to\infty}\frac{1}{t}\left(\cos^4\left(\frac{\chi}{2}\right)|\tilde{P}_{|g_a e_b\rangle\to(t)|e_a g_b\rangle}|^2 \right. \\ + \sin^4\left(\frac{\chi}{2}\right)|\tilde{P}_{|e_a g_b\rangle\to|g_a e_b\rangle}(t)|^2 \\ - 2\cos^2\left(\frac{\chi}{2}\right)\sin^2\left(\frac{\chi}{2}\right) \\ \left.\times \mathrm{Re}[\tilde{P}_{|g_a e_b\rangle\to|e_a g_b\rangle}(t)\tilde{P}^*_{|e_a g_b\rangle\to|g_a e_b\rangle}(t)]\right). \end{aligned} \tag{C12}$$

Using the definitions in (C9), we obtain

$$
\begin{aligned}
W &= \lim_{t\to\infty}\frac{1}{t}\left(\cos^4\left(\frac{\chi}{2}\right)P_{|g_ae_b\rangle\to|e_ag_b\rangle}(t)+\sin^4\left(\frac{\chi}{2}\right)P_{|e_ag_b\rangle\to|g_ae_b\rangle}(t)-2\cos^2\left(\frac{\chi}{2}\right)\sin^2\left(\frac{\chi}{2}\right)\right.\\
&\quad\left.\times\,\mathrm{Re}[\tilde{P}_{|g_ae_b\rangle\to|e_ag_b\rangle}(t)\tilde{P}^*_{|e_ag_b\rangle\to|g_ae_b\rangle}(t)]\right),\\
&=\cos^4\left(\frac{\chi}{2}\right)\lim_{t\to\infty}\frac{P_{|g_ae_b\rangle\to|e_ag_b\rangle}(t)}{t}+\sin^4\left(\frac{\chi}{2}\right)\lim_{t\to\infty}\frac{P_{|e_ag_b\rangle\to|g_ae_b\rangle}(t)}{t}-2\cos^2\left(\frac{\chi}{2}\right)\sin^2\left(\frac{\chi}{2}\right)\\
&\quad\times\lim_{t\to\infty}\frac{\mathrm{Re}[\tilde{P}_{|g_ae_b\rangle\to|e_ag_b\rangle}(t)\tilde{P}^*_{|e_ag_b\rangle\to|g_ae_b\rangle}(t)]}{t},\\
&=\cos^4\left(\frac{\chi}{2}\right)W_{|g_ae_b\rangle\to|e_ag_b\rangle}+\sin^4\left(\frac{\chi}{2}\right)W_{|e_ag_b\rangle\to|g_ae_b\rangle}-2\cos^2\left(\frac{\chi}{2}\right)\sin^2\left(\frac{\chi}{2}\right)\lim_{t\to\infty}\frac{1}{t}\mathrm{Re}[\tilde{P}_{|g_ae_b\rangle\to|e_ag_b\rangle}\tilde{P}^*_{|e_ag_b\rangle\to|g_ae_b\rangle}].
\end{aligned}
\tag{C13}
$$

This last result shows how the transition rate depends on the individual transition rates $W_{|a\rangle\to|b\rangle}$ plus a correction given by the quantum interference between the states. Moreover, each term is normalized by a factor that depends on how the system is initially prepared. As mentioned previously, this result is similar to the expanded expression $P_s = |A_{\mathrm{path},1}|^2 + |A_{\mathrm{path},2}|^2 - \mathrm{Re}[A^*_{\mathrm{path},1}A_{\mathrm{path},2}]$. Since P_s is calculated in terms of quantum amplitudes, the final P_s expression presents a *classical* counterpart, linked with the qubit path probabilities $P_s = |A_{\mathrm{path},i}|^2$, along with a *quantum* counterpart, linked with the interference term $\mathrm{Re}[A^*_{\mathrm{path},1}A_{\mathrm{path},2}]$. Analogously to the disordered systems, the interference term survives disorder averaging when the system presents time-reversal symmetry. In this way, the term $\langle\mathrm{Re}[A^*_{\mathrm{path},1}A_{\mathrm{path},2}]\rangle$ depicts a negative correction to the surviving probability $\langle P_s\rangle$, i.e., the transition probability $\langle W\rangle$, with $\langle\cdot\rangle$ representing the disorder averaging.

We still need to calculate the unknown quantities $W_{|g_ae_b\rangle\to|e_ag_b\rangle}$, $W_{|e_ag_b\rangle\to|g_ae_b\rangle}$, and $\mathrm{Re}[\tilde{P}_{|g_ae_b\rangle\to|e_ag_b\rangle}(t)\,\tilde{P}^*_{|e_ag_b\rangle\to|g_ae_b\rangle}(t)]$ in terms of the driving parameters. The first step is to calculate $\Delta(t) = \Delta e^{-i\phi(t)}$. To this end, we use the Bessel function property $e^{ix\sin(\theta)} = \sum_n J_n(x)e^{in\theta}$, $n\in\mathbb{Z}$, to obtain

$$
\Delta(t) = \Delta\sum_{nm}J_n\left(\frac{A_1}{\omega_1}\right)J_m\left(\frac{A_2}{\omega_2}\right)e^{i(\varepsilon_0+n\omega_1+m\omega_2)t}e^{im\alpha}.
\tag{C14}
$$

Substituting Eq. (C14) into Eqs. (C9) and (C10), it follows that

$$
\begin{aligned}
P_{|g_ae_b\rangle\to|e_ag_b\rangle}(t) &= \frac{\Delta^2}{4}\sum_{nmn'm'}J_n\left(\frac{A_1}{\omega_1}\right)J_m\left(\frac{A_2}{\omega_2}\right)J_{n'}\left(\frac{A_1}{\omega_1}\right)J_{m'}\left(\frac{A_2}{\omega_2}\right)e^{im\alpha}e^{-im'\alpha}e^{i((n-n')\omega_1+(m-m')\omega_2)t/2}\\
&\quad\times\frac{\sin(\varepsilon_0+n\omega_1+m\omega_2)t/2}{(\varepsilon_0+n\omega_1+m\omega_2)/2}\frac{\sin(\varepsilon_0+n'\omega_1+m'\omega_2)t/2}{(\varepsilon_0+n'\omega_1+m'\omega_2)/2}.
\end{aligned}
\tag{C15}
$$

The interference term can be written as

$$
\begin{aligned}
\mathrm{Re}[\tilde{P}_{|g_ae_b\rangle\to|e_ag_b\rangle}(t)\tilde{P}^*_{|e_ag_b\rangle\to|g_ae_b\rangle}(t)] &= \frac{\Delta^2}{4}\mathrm{Re}\left[\sum_{nmn'm'}J_n\left(\frac{A_1}{\omega_1}\right)J_m\left(\frac{A_2}{\omega_2}\right)J_{n'}\left(\frac{A_1}{\omega_1}\right)J_{m'}\left(\frac{A_2}{\omega_2}\right)e^{im\alpha}e^{im'\alpha}e^{i((n+n')\omega_1+(m+m')\omega_2)t/2}\right.\\
&\quad\left.\times\frac{\sin(\varepsilon_0+n\omega_1+m\omega_2)t/2}{(\varepsilon_0+n\omega_1+m\omega_2)/2}\frac{\sin(\varepsilon_0+n'\omega_1+m'\omega_2)t/2}{(\varepsilon_0+n'\omega_1+m'\omega_2)/2}\right].
\end{aligned}
\tag{C16}
$$

At this point, it should be noted that the calculations above are different from [23,25,27], since in our case the frequency ω of driving is small compared to the energy gap Δ; thus, it is not possible to neglect the fast oscillating terms. In this way, the final calculations are slightly different.

For simplicity, we consider the limit when $\alpha \to 0$; thus, $e^{im\alpha} \approx 1 + im\alpha$. From Eq. (C15) we obtain

$$\begin{aligned} P_{|g_a e_b\rangle \to |e_a g_b\rangle}(t) \approx{}& \frac{\Delta^2}{4}\left|\sum_{nm} J_n\left(\frac{A_1}{\omega_1}\right) J_m\left(\frac{A_2}{\omega_2}\right) e^{i((n\omega_1+m\omega_2)t/2} \frac{\sin(\varepsilon_0+n\omega_1+m\omega_2)t/2}{(\varepsilon_0+n\omega_1+m\omega_2)/2}\right|^2 \\ &+ \frac{\Delta^2}{4}\alpha^2\left|\sum_{nm} m J_n\left(\frac{A_1}{\omega_1}\right) J_m\left(\frac{A_2}{\omega_2}\right) e^{i((n\omega_1+m\omega_2)t/2} \frac{\sin(\varepsilon_0+n\omega_1+m\omega_2)t/2}{(\varepsilon_0+n\omega_1+m\omega_2)/2}\right|^2 \\ &+ \frac{\Delta^2}{4} i\alpha \sum_{nmn'm'} (m-m') J_n\left(\frac{A_1}{\omega_1}\right) J_m\left(\frac{A_2}{\omega_2}\right) J_{n'}\left(\frac{A_1}{\omega_1}\right) J_{m'}\left(\frac{A_2}{\omega_2}\right) e^{i((n-n')\omega_1+(m-m')\omega_2)t/2} \\ &\times \frac{\sin(\varepsilon_0+n\omega_1+m\omega_2)t/2}{(\varepsilon_0+n\omega_1+m\omega_2)/2} \frac{\sin(\varepsilon_0+n'\omega_1+m'\omega_2)t/2}{(\varepsilon_0+n'\omega_1+m'\omega_2)/2}. \end{aligned} \tag{C17}$$

Taking the limit $\lim_{t\to\infty} P_{|g_a e_b\rangle \to |e_a g_b\rangle}(t)/t$ and using the well-known result $\lim_{t\to\infty}(1/t)[\sin^2(\beta t)/\beta^2] \to 2\pi\delta(\beta)$, the corresponding transition rate can be approximately calculated as

$$\begin{aligned} W_{|g_a e_b\rangle \to |e_a g_b\rangle} = \lim_{t\to\infty} \frac{P_{|g_a e_b\rangle \to |e_a g_b\rangle}(t)}{t} \approx{}& \frac{\Delta^2}{4} \sum_{nm} J_n\left(\frac{A_1}{\omega_1}\right)^2 J_m\left(\frac{A_2}{\omega_2}\right)^2 \delta(\varepsilon_0+n\omega_1+m\omega_2) \\ &+ \frac{\Delta^2}{4}\alpha^2 \sum_{nm} m^2 J_n\left(\frac{A_1}{\omega_1}\right)^2 J_m\left(\frac{A_2}{\omega_2}\right)^2 \delta(\varepsilon_0+n\omega_1+m\omega_2) \approx W^{\alpha=0}_{|g_a e_b\rangle \to |e_a g_b\rangle} + \alpha^2 \xi^{\alpha\neq 0}_{|g_a e_b\rangle \to |e_a g_b\rangle}. \end{aligned} \tag{C18}$$

Using the same procedure presented above to calculate the interference term, we obtain

$$\begin{aligned} &\lim_{t\to\infty} \frac{1}{t} \mathrm{Re}[\tilde{P}_{|g_a e_b\rangle \to |e_a g_b\rangle}(t) \tilde{P}^*_{|e_a g_b\rangle \to |g_a e_b\rangle}(t)] \\ &\approx \frac{\Delta^2}{4} \lim_{t\to\infty} \frac{1}{t} \mathrm{Re}\left[\left\{\sum_{nm} J_n\left(\frac{A_1}{\omega_1}\right) J_m\left(\frac{A_2}{\omega_2}\right) e^{i((n\omega_1+m\omega_2)t/2} \frac{\sin(\varepsilon_0+n\omega_1+m\omega_2)t/2}{(\varepsilon_0+n\omega_1+m\omega_2)/2}\right\}^2\right] \\ &- \frac{\Delta^2}{4}\alpha^2 \lim_{t\to\infty} \frac{1}{t} \mathrm{Re}\left[\left\{\sum_{nm} m J_n\left(\frac{A_1}{\omega_1}\right) J_m\left(\frac{A_2}{\omega_2}\right) e^{i(n\omega_1+m\omega_2)t/2} \frac{\sin(\varepsilon_0+n\omega_1+m\omega_2)t/2}{(\varepsilon_0+n\omega_1+m\omega_2)/2}\right\}^2\right] \\ &\approx \frac{\Delta^2}{4} \sum_{nm} J_n\left(\frac{A_1}{\omega_1}\right)^2 J_m\left(\frac{A_2}{\omega_2}\right)^2 \delta(\varepsilon_0+n\omega_1+m\omega_2) \\ &- \frac{\Delta^2}{4}\alpha^2 \sum_{nm} m^2 J_n\left(\frac{A_1}{\omega_1}\right)^2 J_m\left(\frac{A_2}{\omega_2}\right)^2 \delta(\varepsilon_0+n\omega_1+m\omega_2) \\ &\approx \lim_{t\to\infty} \frac{1}{t} \mathrm{Re}[\tilde{P}_{|g_a e_b\rangle \to |e_a g_b\rangle}(t) \tilde{P}^*_{|e_a g_b\rangle \to |g_a e_b\rangle}(t)]^{\alpha=0} - \alpha^2 \eta^{\alpha\neq 0}. \end{aligned} \tag{C19}$$

Finally, from Eqs. (C18) and (C19) we obtain an approximated equation for the total transition rate around the point $\alpha \approx 0$, which reads

$$\begin{aligned} W \approx{}& \left[\cos^4\left(\frac{\chi}{2}\right) W^{\alpha=0}_{|g_a e_b\rangle \to |e_a g_b\rangle} + \sin^4\left(\frac{\chi}{2}\right) W^{\alpha=0}_{|e_a g_b\rangle \to |g_a e_b\rangle} - 2\cos^2\left(\frac{\chi}{2}\right)\sin^2\left(\frac{\chi}{2}\right) \lim_{t\to\infty} \frac{1}{t} \mathrm{Re}[\tilde{P}_{|g_a e_b\rangle \to |e_a g_b\rangle} \tilde{P}^*_{|e_a g_b\rangle \to |g_a e_b\rangle}]^{\alpha=0}\right] \\ &+ \alpha^2 \left[\cos^4\left(\frac{\chi}{2}\right) \xi^{\alpha\neq 0}_{|g_a e_b\rangle \to |e_a g_b\rangle} + \sin^4\left(\frac{\chi}{2}\right) \xi^{\alpha\neq 0}_{|e_a g_b\rangle \to |g_a e_b\rangle} + 2\cos^2\left(\frac{\chi}{2}\right)\sin^2\left(\frac{\chi}{2}\right) \eta^{\alpha\neq 0}\right], \end{aligned} \tag{C20}$$

$$\approx W_{\alpha=0} + \alpha^2 \zeta_{\alpha\neq 0}. \tag{C21}$$

Applying the average over initial conditions to Eq. (C21), we obtain the general equation

$$\begin{aligned}\langle W\rangle &\approx \langle W\rangle_{\alpha=0} + \alpha^2\langle\zeta\rangle_{\alpha\neq 0},\\ \langle W\rangle - \langle W\rangle_{\alpha=0} &\approx \alpha^2\langle\zeta\rangle_{\alpha\neq 0},\end{aligned} \tag{C22}$$

defining the averaged transition rate as $\langle W\rangle = 1/(|\varepsilon_{0,\max} - \varepsilon_{0,\min}|)\int_{\varepsilon_{0,\min}}^{\varepsilon_{0,\max}} W\,d\varepsilon_0$, where $\langle W\rangle_{\alpha=0}$ and $\langle\zeta\rangle_{\alpha\neq 0}$ are positive quantities. From this result, we conclude that the observation of weak localization in this system is possible.

APPENDIX D: QUANTUM SIMULATOR AND RANDOM MATRIX THEORY PREDICTIONS FOR DISORDERED MESOSCOPIC SYSTEMS

In this section we review the WL and UCFs predicted by random matrix theory (RMT) [40] for disordered mesoscopic systems, with the aim to compare the results with those we obtain for the quantum simulator.

By assuming a diffusive (or fully chaotic billiard) transport regime [38], the suppression of the WL correction in the average conductance $\langle G\rangle$ follows a Lorentzian shape, i.e.,

$$\langle G\rangle(B) = a - \frac{b}{1+(B/B_c)^2}, \tag{D1}$$

where B is the external magnetic field, B_c is the critical magnetic field, and $a, b \in \mathbb{R}$ are parameters depending on the system characteristics. In our case, we find that the average transition rate $\langle W\rangle$ satisfies

$$\langle W\rangle_\alpha = \tilde{a} - \frac{\tilde{b}}{1+(\alpha/\alpha_c)^2}, \tag{D2}$$

where α is the time reversal breaking control parameter and α_c is the critical parameter playing the role of the critical magnetic field in Eq. (D1). In this last case $\tilde{a}, \tilde{b} \in \mathbb{R}$ are constants depending on the properties of the quantum simulator. Fitting Eq. (D2) with the numerical results, we obtain $\alpha_c = (0.09 \pm 0.03)$. Figure 6 displays the fitting curve along with the numerical and experimental results, showing good agreement.

A Taylor expansion of Eq. (D2) around $\alpha \sim 0$ yields

$$\langle W\rangle_\alpha \sim \tilde{c} + \frac{b}{\alpha_c^2}\alpha^2 \tag{D3}$$

with $\tilde{c} = \tilde{a} - \tilde{b}$. Note that Eq. (D3) is similar to the analytical expression obtained in Eq. (C22).

It should be stressed that as our quantum simulator operates in the limit of few scattering centers, the RMT predictions valid for a highly disordered transport regime are not necessarily fulfilled. In particular, in Ref. [41] it was shown that the WL correction can follow a dependence of the form $|B|$ for a nonfully chaotic regime.

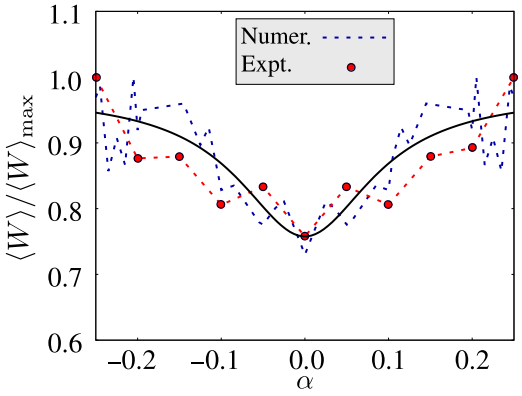

FIG. 6. First-order statistics of the transition rate: WL. Experimental and numerical results of the normalized transition rate $\langle W\rangle/\langle W\rangle_{\max}$ as a function of the asymmetry parameter α. Here $\langle W\rangle$ is the transition rate ensemble averaged over all $f_{\rm dc}$ values for fixed α, and $\langle W\rangle_{\max}$ is the corresponding maximum value for each case. The fitting curve using Eq. (D2) is plotted with a solid line.

The RMT predictions for the circular orthogonal ensemble (COE) [time-reversal symmetry (TRS)] and circular unitary ensemble (CUE) (non-TRS) ensembles [7,8] satisfy $\langle\delta G^2\rangle_{\rm TRS} \sim 2\langle\delta G^2\rangle_{\text{non-TRS}}$, with $\text{var}(G) = \langle\delta G^2\rangle$. In our case, in order to perform a similar comparison, we define the average fluctuation $\overline{[\langle\delta W^2\rangle/\langle W\rangle^2]}_{\rm norm}$ for different α values satisfying $\alpha \neq> \alpha_c$ in order to consider the non-TRS case, and after fitting with Eq. (D2) we obtain

$$\begin{aligned}&\left(\overline{\left[\frac{\langle\delta W^2\rangle}{\langle W\rangle^2}\right]}_{\rm norm}\right)_{\alpha>\alpha_c}\\ &\quad\sim 0.8139 \quad \text{for the experimental results,}\\ &\left(\overline{\left[\frac{\langle\delta W^2\rangle}{\langle W\rangle^2}\right]}_{\rm norm}\right)_{\alpha>\alpha_c} \sim 0.8136 \quad \text{for the numerical results.}\end{aligned} \tag{D4}$$

In Fig. 7 we display the experimental and numerical results of the UCFs as a function of α. The value $(\overline{[\langle\delta W^2\rangle/\langle W\rangle^2]}_{\rm norm})_{\alpha>\alpha_c} \sim 0.8$ is plotted with a red solid line. Note that the ratio $\langle\delta W^2\rangle_{\alpha=0}/\langle\delta W^2\rangle_{\alpha>\alpha_c} \sim 2$ is satisfied for both the numerical and experimental results. The arrows schematically plotted in Fig. 7 show that the averaged fluctuations and the UCFs peak are measured from the minimum value of $[\langle\delta W^2\rangle/\langle W\rangle^2]_{\rm norm}$ instead of from zero.

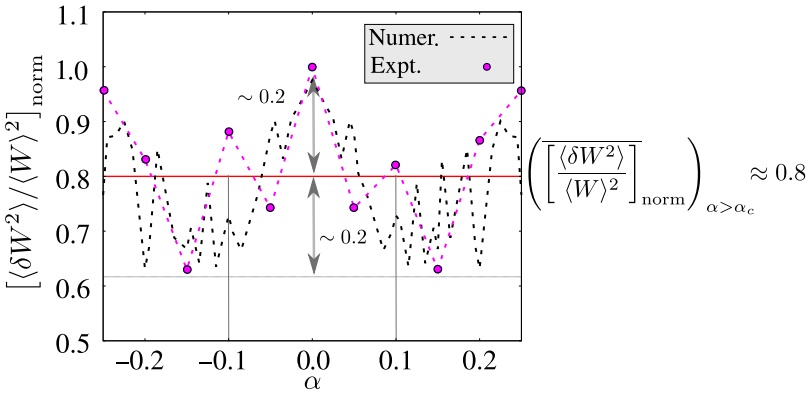

FIG. 7. Second-order statistics of the transition rate: UCFs. Experimental and numerical results for the normalized variance $[\langle \delta W^2\rangle/\langle W\rangle^2]_{\rm norm}$. The average of the fluctuations when $\alpha \neq 0$ is plotted with a solid red line, corresponding to the amount $(\overline{[\langle \delta W^2\rangle/\langle W\rangle^2]_{\rm norm}})_{\alpha>\alpha_c} \sim 0.8$ for both the numerical and experimental results; see Eq. (D4).

In the case of the COE ensemble [40], the WL and UCFs respectively satisfy

$$\langle G\rangle_{\rm TRS} = -\frac{2}{3}\left(\frac{e^2}{h}\right), \qquad \langle \delta G^2\rangle_{\rm TRS} = \frac{2}{15}\left(\frac{e^2}{h}\right)^2. \tag{D5}$$

In order to compare these typical values with our results, we define the dimensionless ratio

$$r_{\rm RMT} = \left(\frac{\langle \delta G^2\rangle}{\langle G\rangle^2}\right)_{\rm TRS} = \frac{3}{10} \sim 0.3. \tag{D6}$$

In our case, taking into account the previous results, the ratio gives

$$r = \left(\frac{\langle \delta W^2\rangle}{\langle W\rangle^2}\right)_{\alpha=0} \sim 0.5585 \quad \text{for the experimental results,}$$
$$r = \left(\frac{\langle \delta W^2\rangle}{\langle W\rangle^2}\right)_{\alpha=0} \sim 0.6958 \quad \text{for the numerical results,} \tag{D7}$$

with r being the order of $r_{\rm RMT}$.

[1] E. Abrahams, P. W. Anderson, D. C. Licciardello, and T. V. Ramakrishnan, Scaling Theory of Localization: Absence of Quantum Diffusion in Two Dimensions, Phys. Rev. Lett. **42**, 673 (1979).

[2] Patrick A. Lee and T. V. Ramakrishnan, Disordered electronic systems, Rev. Mod. Phys. **57**, 287 (1985).

[3] Boris L. Al'tshuler and Patrick A. Lee, Quantum mechanical coherence of electron wavefunctions in materials with imperfections has led to major revisions in the theory of electrical conductivity and to novel phenomena in submicron devices, Phys. Today **41**, No. 12, 36 (1988).

[4] R. A. Webb, S. Washburn, C. P. Umbach, and R. B. Laibowitz, Observation of $\frac{h}{e}$ Aharonov-Bohm Oscillations in Normal-Metal Rings, Phys. Rev. Lett. **54**, 2696 (1985).

[5] P. A. Lee and A. D. Stone, Universal Conductance Fluctuations in Metals, Phys. Rev. Lett. **55**, 1622 (1985).

[6] A. Benoit, C. P. Umbach, R. B. Laibowitz, and R. A. Webb, Length-Independent Voltage Fluctuations in Small Devices, Phys. Rev. Lett. **58**, 2343 (1987).

[7] Supriyo Datta, *Electronic Transport in Mesoscopic Systems*, Cambridge Studies in Semiconductor Physics and Microelectronic Engineering (Cambridge University Press, Cambridge, 1995).

[8] David Ferry and Stephen Marshall Goodnick, *Transport in Nanostructures*, Cambridge Studies in Semiconductor Physics and Microelectronic Engineering (Cambridge University Press, Cambridge, 1997).

[9] Gerd Bergmann, Quantitative analysis of weak localization in thin mg films by magnetoresistance measurements, Phys. Rev. B **25**, 2937 (1982).

[10] S Washburn and R. A. Webb, Quantum transport in small disordered samples from the diffusive to the ballistic regime, Rep. Prog. Phys. **55**, 1311 (1992).

[11] G. J. Dolan and D. D. Osheroff, Nonmetallic Conduction in Thin Metal Films at Low Temperatures, Phys. Rev. Lett. **43**, 721 (1979).

[12] D. J. Bishop, D. C. Tsui, and R. C. Dynes, Nonmetallic Conduction in Electron Inversion Layers at Low Temperatures, Phys. Rev. Lett. **44**, 1153 (1980).

[13] Yu Chen, P. Roushan, D. Sank, C. Neill, Erik Lucero, Matteo Mariantoni, R. Barends, B. Chiaro, J. Kelly, A. Megrant, J. Y. Mutus, P. J. J. O'Malley, A. Vainsencher, J. Wenner, T. C. White, Yi Yin, A. N. Cleland, and John M. Martinis, Emulating weak localization using a solid-state quantum circuit, Nat. Commun. **5**, 5184 (2014).

[14] C. M. Marcus, A. J. Rimberg, R. M. Westervelt, P. F. Hopkins, and A. C. Gossard, Conductance Fluctuations and Chaotic Scattering in Ballistic Microstructures, Phys. Rev. Lett. **69**, 506 (1992).

[15] I. H. Chan, R. M. Clarke, C. M. Marcus, K. Campman, and A. C. Gossard, Ballistic Conductance Fluctuations in Shape Space, Phys. Rev. Lett. **74**, 3876 (1995).

[16] J. A. Folk, S. R. Patel, S. F. Godijn, A. G. Huibers, S. M. Cronenwett, C. M. Marcus, K. Campman, and A. C. Gossard, Statistics and Parametric Correlations of Coulomb Blockade Peak Fluctuations in Quantum Dots, Phys. Rev. Lett. **76**, 1699 (1996).

[17] S. V. Morozov, K. S. Novoselov, M. I. Katsnelson, F. Schedin, L. A. Ponomarenko, D. Jiang, and A. K. Geim,

Strong Suppression of Weak Localization in Graphene, Phys. Rev. Lett. **97**, 016801 (2006).
[18] Meint P. Van Albada and Ad Lagendijk, Observation of Weak Localization of Light in a Random Medium, Phys. Rev. Lett. **55**, 2692 (1985).
[19] Pierre-Etienne Wolf and Georg Maret, Weak Localization and Coherent Backscattering of Photons in Disordered Media, Phys. Rev. Lett. **55**, 2696 (1985).
[20] Frank Scheffold and Georg Maret, Universal Conductance Fluctuations of Light, Phys. Rev. Lett. **81**, 5800 (1998).
[21] A. Schreiber, K. N. Cassemiro, V. Potoček, A. Gábris, P. J. Mosley, E. Andersson, I. Jex, and Ch. Silberhorn, Photons Walking the Line: A Quantum Walk with Adjustable Coin Operations, Phys. Rev. Lett. **104**, 050502 (2010).
[22] Simon Gustavsson, Jonas Bylander, and William D. Oliver, Time-Reversal Symmetry and Universal Conductance Fluctuations in a Driven Two-Level System, Phys. Rev. Lett. **110**, 016603 (2013).
[23] Alejandro Ferrón, Daniel Domínguez, and María José Sánchez, Mesoscopic fluctuations in biharmonically driven flux qubits, Phys. Rev. B **95**, 045412 (2017).
[24] William D. Oliver, Yang Yu, Janice C. Lee, Karl K. Berggren, Leonid S. Levitov, and Terry P. Orlando, Mach-zehnder interferometry in a strongly driven superconducting qubit, Science **310**, 1653 (2005).
[25] D. M. Berns, W. D. Oliver, S. O. Valenzuela, A. V. Shytov, K. K. Berggren, L. S. Levitov, and T. P. Orlando, Coherent Quasiclassical Dynamics of a Persistent Current Qubit, Phys. Rev. Lett. **97**, 150502 (2006).
[26] Sergio O. Valenzuela, William D. Oliver, David M. Berns, Karl K. Berggren, Leonid S. Levitov, and Terry P. Orlando, Microwave-induced cooling of a superconducting qubit, Science **314**, 1589 (2006).
[27] David M. Berns, Mark S. Rudner, Sergio O. Valenzuela, Karl K. Berggren, William D. Oliver, Leonid S. Levitov, and Terry P. Orlando, Amplitude spectroscopy of a solid-state artificial atom, Nature **455**, 51 (2008).
[28] M. S. Rudner, A. V. Shytov, L. S. Levitov, D. M. Berns, W. D. Oliver, S. O. Valenzuela, and T. P. Orlando, Quantum Phase Tomography of a Strongly Driven Qubit, Phys. Rev. Lett. **101**, 190502 (2008).
[29] Jens Koch, Terri M. Yu, Jay Gambetta, A. A. Houck, D. I. Schuster, J. Majer, Alexandre Blais, M. H. Devoret, S. M. Girvin, and R. J. Schoelkopf, Charge-insensitive qubit design derived from the cooper pair box, Phys. Rev. A **76**, 042319 (2007).
[30] Yun-Pil Shim and Charles Tahan, Semiconductor-inspired design principles for superconducting quantum computing, Nat. Commun. **7**, 11059 (2016).
[31] Daniel L. Campbell, Yun-Pil Shim, Bharath Kannan, Roni Winik, David Kim, Jonilyn Yoder, Charles Tahan, Simon Gustavsson, and William D. Oliver, Composite qubit approach to superconducting quantum computing using coherent Landau-Zener control (to be published).
[32] R. Barends, J. Kelly, A. Megrant, D. Sank, E. Jeffrey, Y. Chen, Y. Yin, B. Chiaro, J. Mutus, C. Neill, P. O'Malley, P. Roushan, J. Wenner, T. C. White, A. N. Cleland, and John M. Martinis, Coherent Josephson Qubit Suitable for Scalable Quantum Integrated Circuits, Phys. Rev. Lett. **111**, 080502 (2013).
[33] M. D. Hutchings, J. B. Hertzberg, Y. Liu, N. T. Bronn, G. A. Keefe, Markus Brink, Jerry M. Chow, and B. L. T. Plourde, Tunable Superconducting Qubits with Flux-Independent Coherence, Phys. Rev. Appl. **8**, 044003 (2017).
[34] T. P. Orlando, J. E. Mooij, Lin Tian, Caspar H. van der Wal, L. S. Levitov, Seth Lloyd, and J. J. Mazo, Superconducting persistent-current qubit, Phys. Rev. B **60**, 15398 (1999).
[35] I. Chiorescu, Y. Nakamura, C. J. P. M. Harmans, and J. E. Mooij, Coherent quantum dynamics of a superconducting flux qubit, Science **299**, 1869 (2003).
[36] Jonas Bylander, Simon Gustavsson, Fei Yan, Fumiki Yoshihara, Khalil Harrabi, George Fitch, David G. Cory, Yasunobu Nakamura, Jaw-Shen Tsai, and William D. Oliver, Noise spectroscopy through dynamical decoupling with a superconducting flux qubit, Nat. Phys. **7**, 565 (2011).
[37] S. N. Shevchenko, S. Ashhab, and Franco Nori, Landau-Zener-stückelberg interferometry, Phys. Rep. **492**, 1 (2010).
[38] Harold U. Baranger, Rodolfo A. Jalabert, and A. D. Stone, Weak Localization and Integrability in Ballistic Cavities, Phys. Rev. Lett. **70**, 3876 (1993).
[39] Waltraut Wustmann, Ph.D. thesis, Technische Universität, Dresden, 2010.
[40] C. W. J. Beenakker and J. A. Melsen, Conductance fluctuations, weak localization, and shot noise for a ballistic constriction in a disordered wire, Phys. Rev. B **50**, 2450 (1994).
[41] C. W. J. Beenakker, Random-matrix theory of quantum transport, Rev. Mod. Phys. **69**, 731 (1997).